

Article

A Hybrid SVR-Based Prediction Model for the Interfacial Bond Strength of Externally Bonded FRP Laminates on Grooves with Concrete Prisms

Kaffayatullah Khan ^{1,*} , Mudassir Iqbal ² , Rahul Biswas ³ , Muhammad Nasir Amin ¹ , Sajid Ali ⁴ , Jitendra Gudainiyan ⁵ , Anas Abdulalim Alabdullah ¹  and Abdullah Mohammad Abu Arab ¹

- ¹ Department of Civil and Environmental Engineering, College of Engineering, King Faisal University, Al-Ahsa 31982, Saudi Arabia; mgadir@kfu.edu.sa (M.N.A.); 218038024@student.kfu.edu.sa (A.A.A.); 219041496@student.kfu.edu.sa (A.M.A.A.)
- ² Department of Civil Engineering, University of Engineering and Technology, Peshawar 25120, Pakistan; mudassiriqbal@uetpeshawaitr.edu.pk
- ³ Department of Applied Mechanics, Visvesvaraya National Institute of Technology Nagpur, Nagpur 440010, India; rahulbiswas@apm.vnit.ac.in
- ⁴ Mechanical and Energy Engineering, College of Engineering, Imam Abdulrahman Bin Faisal University, P.O. Box 1982, Dammam 31451, Saudi Arabia; sakzada@iau.edu.sa
- ⁵ Department of Civil Engineering, GLA University, Mathura 281406, India; jitendra.gudainiyan@gla.ac.in
- * Correspondence: kkhan@kfu.edu.sa

Abstract: The current work presents a comparative study of hybrid models that use support vector machines (SVMs) and meta-heuristic optimization algorithms (MOAs) to predict the ultimate interfacial bond strength (IBS) capacity of fiber-reinforced polymer (FRP). More precisely, a dataset containing 136 experimental tests was first collected from the available literature for the development of hybrid SVM models. Five MOAs, namely the particle swarm optimization, the grey wolf optimizer, the equilibrium optimizer, the Harris hawks optimization and the slime mold algorithm, were used; five hybrid SVMs were constructed. The performance of the developed SVMs was then evaluated. The accuracy of the constructed hybrid models was found to be on the higher side, with R^2 ranges between 0.8870 and 0.9774 in the training phase and between 0.8270 and 0.9294 in the testing phase. Based on the experimental results, the developed SVM-HHO (a hybrid model that uses an SVM and the Harris hawks optimization) was overall the most accurate model, with R^2 values of 0.9241 and 0.9241 in the training and testing phases, respectively. Experimental results also demonstrate that the developed hybrid SVM can be used as an alternate tool for estimating the ultimate IBS capacity of FRP concrete in civil engineering projects.

Keywords: interfacial bond strength; fiber-reinforced polymer; single-lap shear test; support vector machine; meta-heuristic optimization algorithms



Citation: Khan, K.; Iqbal, M.; Biswas, R.; Amin, M.N.; Ali, S.; Gudainiyan, J.; Alabdullah, A.A.; Arab, A.M.A. A Hybrid SVR-Based Prediction Model for the Interfacial Bond Strength of Externally Bonded FRP Laminates on Grooves with Concrete Prisms.

Polymers **2022**, *14*, 3097. <https://doi.org/10.3390/polym14153097>

Academic Editors: T. Tafsirojaman and Prabir K. Sarker

Received: 2 June 2022

Accepted: 14 July 2022

Published: 29 July 2022

Publisher's Note: MDPI stays neutral with regard to jurisdictional claims in published maps and institutional affiliations.



Copyright: © 2022 by the authors. Licensee MDPI, Basel, Switzerland. This article is an open access article distributed under the terms and conditions of the Creative Commons Attribution (CC BY) license (<https://creativecommons.org/licenses/by/4.0/>).

1. Introduction

As a result of the corrosion of traditional steel reinforcement, reinforced concrete (RC) structures are required to undergo regular maintenance and repair [1]. Therefore, strengthening existing structures is regarded as an increasing priority in the construction industry, as it is necessary in order to comply with improved code designs and strength criteria [2]. Hence, fiber-reinforced polymer (FRP) laminates are increasingly being employed for the purpose of retrofitting and improving the current structural capacity of beams [3–5], columns [6,7] and beam–column junctions [8–11] due to their high performance.

FRP plates may potentially replace steel plates in structural reinforcement due to their light weight and high strength, as well as their superior resistance to corrosion [12], creep/fatigue [13] and hygrothermal stresses [14]. However, notwithstanding those benefits, FRP incorporation has some disadvantages, such as rupture, concrete crushing,

shear cracks and debonding between concrete and laminates that propagates through FRP-strengthened structures and causes more damage [15–17]. FRP rupture or concrete crushing may occur if the ends of the reinforcing plates are not properly anchored [18]. Even before reaching full capacity, premature debonding can be observed and is the most common recorded failure; it leads to the debonding of the FRP laminate and progresses towards the center from the ends [19]. The diffusion of water molecules into the FRP plate may produce irreversible interfacial debonding, resulting in a reduction in the interlaminar shear strength of the FRP plate. Increased temperatures can also aggravate debonding [14]. There may be interfacial FRP debonding as a result of dynamic loads and thermal aging [20]. Strengthened constructions lose structural capacity when FRP laminates debond from one another, and this is a serious problem [16]. In FRP-strengthened RC members, early plate debonding from the concrete prism has been found in experiments. The composite action between an FRP component and a concrete prism determines the failure model of a reinforced component. Plate-end debonding and intermediate crack-induced debonding may occur if the composite process between the FRP and the concrete continues [21]. Interfacial bond failures can also be caused by poor bond quality due to poor workmanship [22].

Existing laboratory studies have demonstrated that improper preparation of the concrete-to-FRP interface is the most significant cause of early failure in the form of FRP debonding [23]. It is possible to increase the strength of the bond between FRP and concrete in several ways, including epoxy interlocking near the surface mounting. The need for a flexible interface between concrete and FRP laminate for the flexural strengthening of a beam has therefore been identified as a key requirement. Removing the damaged surface layer of the concrete and exposing the coarse aggregate is a part of the surface preparation process. As a result, the final rupture strength is increased due to the delayed debonding of the FRP sheet from the concrete surface. The concrete is sandblasted, the dust is removed with a brush and solvents are used to clean the surface; then, the FRP sheets are installed. Surface mounting techniques are used for FRP strengthening; these include FRP rebars and laminates placed in grooves and packed with high-adhesive materials [24–27]. Another option is to use FRP laminates that are externally bonded to the concrete's surface in grooves (Figure 1b). The surface area, material availability, cost, safety, and need for supporting equipment are the major factors that affect the bond [28]. To quantify interfacial bond strength (IBS), some basic experimental approaches, such as the single-lap shear test (SST), have been utilized because of their reliability and simplicity [29–31]. Previous research has led to the development of empirical and semi-empirical formulations for predicting IBS based on experimental data from SSTs [17,32,33]. These formulations have been found to be reasonably accurate. Despite the fact that the available models' empirical relations have a good level of congruence with the experimental data, these models have not been validated using more recent data. In addition, in order to construct these empirical relations, some fundamental simplifications and assumptions were made [34].

Hence, an alternative method of modeling was needed that could replace those complex empirical relations and give more accurate results. Hence, the application of artificial intelligence came into use. The term "artificial intelligence" (AI) refers to the widespread application of computer programming techniques to solve complex engineering issues, particularly those involving regression and classification [35–53]. AI models are not only trained by using a large number of experimental observations but also validated using a new dataset [44,54]. In addition, there are several successful applications of AI models in the field of composite construction. According to Vu and Hoang [55], the least square support vector machine was able to forecast the punching shear capacity of FRP-reinforced concrete beams with a coefficient of determination (R^2) equal to 0.99. An artificial neural network (ANN) was utilized by Hoang [56] to forecast the punching shear capacity of steel-fiber-reinforced concrete slabs. Research by Abuodeh et al. [57] used neural interpretation diagrams (NIDs) and recursive feature elimination (RFEs) to analyze the shear capability of RC beams.

Finally, in order to improve the efficiency of engineering projects, AI models based on available experimental data are needed to estimate the IBS of FRP plates attached to a concrete prism. Su et al. [58] developed multilinear regression and ANN AI models to forecast the IBS of FRP laminates to a concrete prism for two different cases; without groove (Figure 1a) and with groove (Figure 1b), namely. The training and validation data yielded R^2 values of 0.81 and 0.91, respectively. However, an ANN's inability to define any meaningful relation between model input and output is a fundamental obstacle to its successful deployment in real-world applications [59,60]. Over-fitting and local minimum problems are two further issues that arise while using ANNs [61]. ANNs also have certain inherent limitations. On the other hand, Vapnik invented support vector machines (SVMs), a new artificial intelligence technique that uses statistical learning theory to solve structural engineering issues [62]. SVMs employ the structured risk minimization (SRM) concept, which outperforms the standard empirical risk minimization (ERM) principle used by conventional neural networks in terms of generalization performance [63–67]. The number of local minima, the sparseness of the solution and the number of support vectors are all important parameters in SVMs. Hence, it has been concluded from past studies that the use of hybrid SVMs is a new approach in this area; in the present work, using support vector regression, an attempt was made to forecast the IBS of FRP laminates. Through the use of 136 different experimental SST results, this study investigated the extent to which the SVR model is able to estimate the IBS of FRP laminates that are externally connected to a concrete prism using grooves (the anchorage made on one end of an FRP component to a concrete prism is shown in Figure 1b). In the analysis, we used samples that had been tested using FRP plates aligned in a direction parallel to the groove. On top of that, the parametric analysis and visual interpretation (Taylor diagram) are shown to demonstrate how the input factors affect IBS.

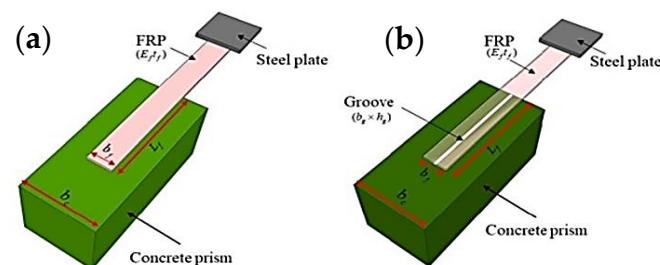


Figure 1. Single-lap shear test: (a) FRP externally bonded on concrete; (b) FRP externally bonded on the grooves of concrete (adapted with permission from Su et al. [58]).

2. Methodology

2.1. Overview of Optimization Algorithms

In this part, meta-heuristic approaches are investigated. In engineering, the use of meta-heuristic optimization algorithms (MOAs) to tackle a variety of issues has grown substantially. They are free gradient methods that can solve highly challenging optimization problems more effectively than conventional approaches [68]. In addition, they are simpler and faster to implement than conventional optimization methods [69]. There are numerous inspiration sources for MOAs, which can be categorized into distinct groups based on these inspiration sources. Among these groups are evolutionary algorithms (EAs), swarm intelligence (SI) methodologies, natural phenomenon approaches and human-inspired algorithms [70,71]. Figure 2 illustrates these divisions. The purpose of the first group of algorithms, known as EAs, is the simulation of natural genetic processes such as crossover, mutation, and selection. This category contains several MOAs, including evolutionary programming [72], evolutionary strategy (ES) [73], the equilibrium optimizer (EO), genetic algorithms [74], decision trees [75] and genetic programming (GP) [76]. The second group, SI, mimics the swarming behavior observed in nature when searching for food. The most notable algorithms in this area include the particle swarm optimization

(PSO) [77], the artificial bee colony (ABC) [78], the grey wolf optimization (GWO) [79], the ant colony optimization (ACO) [80], the salp swarm algorithm (SSA) [81], the marine predators algorithm (MPA) [82], the Harris hawks optimization (HHO) [83], the slime mold algorithm [84] and the whale optimization algorithm (WOA) [85]. This category also includes the spiral optimization (SO) [86], the water cycle algorithm (WCA) [87], the intelligent water drop (IWD) [88], the field of force (FOF) [89] and the electromagnetism algorithm (EA) [90]. Furthermore, extra operations that adhere to physical rules fall under this group. As an illustration, this group includes the field of force (FOF) [91], the electromagnetism algorithm [92], the charged system search (CSS) [93], the gravitational search algorithm (GSA) [94], simulated annealing [95], the aquila optimizer (AO) [96], the electromagnetism-like mechanism, the flow regime algorithm (FRA) [97], the charged system search (CSS) [98], the optics-inspired optimization (OIO) [99] and the chemical reaction. In addition, human activities affect the fourth category [100]. This category includes algorithms such as the teaching–learning-based optimization (TLBO) [101], the volleyball premier league algorithm (VPL) [102], the soccer league competition (SLC) [103], the seeker optimization algorithm (SOA) [104], the league championship algorithm (LCA) [105] and the socio-evolution and learning optimization (SELO) [106].

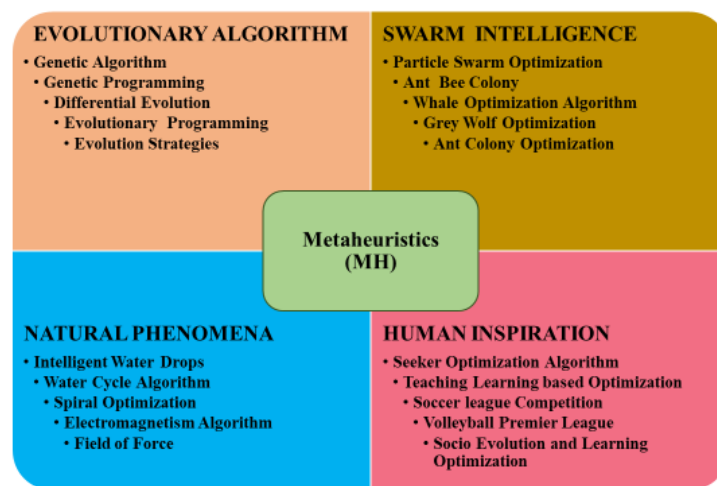


Figure 2. Metaheuristic model classification.

Five distinct SI algorithms, namely PSO, GWO, EO, HHO and SMA, were employed to generate hybrid SVM models in this study. A brief discussion of these OAs is provided in the subsections that follow. This section provides a theoretical background and a short discussion of PSO, GWO, EO, HHO and SMA. Subsequently, the methodological development of hybrid SVMs is presented and discussed. However, before presenting the above details, the working principle of SVMs is briefly presented.

2.2. Support Vector Machines (SVMs)

A Support vector machine (SVM) is a supervised machine learning method that may be used for both regression and classification. It was created by Vapnik in 1995 [107] and is based on statistical learning theory. The SVM technique projects data into a high-dimensional feature space and employs kernels to classify nonlinearly separable datasets [108,109]. In multidimensional space, an SVM model is essentially a representation of various classes in a hyperplane. The SVM generates the hyperplane in an iterative manner in order to reduce errors. The SVM's objective is to split datasets into classes such that a maximum marginal hyperplane (MMH) may be found. The data points closest to the hyperplane, or the points of a dataset that, if deleted, would change the location of the dividing hyperplane, are called support vectors. As a result, they may be regarded as important components of a collection of data. In general, the accuracy of the SVR model is determined by the kernels used and their parameters. The radial basis function

(RBF) has been shown to perform well as a kernel function for SVMs in several forecasting experiments [110–112].

For a dataset $\omega = \{(x_i, y_i) | i = 1, 2, \dots, n\}$ where $x \in R^d$ is a d-dimensional input vector space, and $y \in R$ is an output in a one-dimensional vector space, SVM regression can estimate the relationship between x and y . In the SVM approach, the risk function is minimized by minimizing both empirical risk and $\|\omega\|^2$.

$$R = \frac{1}{2} \|\omega\|^2 + C_C \sum_{i=1}^n l_\epsilon(y_i - f\left(\frac{\rightarrow}{x_i}\right)) \quad (1)$$

where the regression data vector is $\|\omega\|$, and loss is denoted by l_ϵ , which presents the difference between y_i (real output) and $f\left(\frac{\rightarrow}{x_i}\right)$. A positive constant value C_C is needed to fix the prior. $l_\epsilon\left(y_i - f\left(\frac{\rightarrow}{x_i}\right)\right)$ is 0 for $y_i - f\left(\frac{\rightarrow}{x_i}\right) < \epsilon$. Otherwise, it is equal to $y_i - f\left(\frac{\rightarrow}{x_i}\right)$. Minimizing the risk function can be accomplished with the following function:

$$f(x, \alpha, \alpha^*) = \sum_{i=1}^l (\alpha_i^* - \alpha_i) (\varphi(x_i), \varphi(x)) + b \quad (2)$$

where $\alpha_i^* \cdot \alpha_i = 0$ and $\alpha_i^* \cdot \alpha_i \geq 0$; $\varphi(x_i), \varphi(x)$ is a product of the kernel function, and b is a bias term [111].

2.3. Particle Swarm Optimization (PSO)

It was Kennedy and Eberhart [113] who first introduced PSO to the scientific community as part of the swarm-based community in 1995. It is the primary goal of PSO to find global optimal solutions in a multidimensional setting. PSO begins by implementing the random speeds and locations of objects. Next, each object adjusts its position to pick the appropriate status in a multidimensional environment based on its speed, personal best position and global best position. This process continues until the optimal solution is found. It has been determined that the best position that can be gained by individual particles is the ideal status on a global scale; nevertheless, the most desired alternative that can be obtained by the particle is the ideal position on a personal scale. The location of the particle shifts as a result of considering both its optimal personal position and the optimal orientation for its optimal global location. At the same time, the speeds of the objects are altered in accordance with the disparity that exists between their best personal and best global positions. The particles move closer and closer to the optimal location as a result of a combination of exploring and exploiting. The acceleration coefficients c_1 (cognitive coefficient) and c_2 (social coefficient), which have fixed values of 1 and 2, respectively, are dependent on the situation at hand and reflect the level of confidence an element possesses in comparison to its personal and global status. Previous studies [114] provide information regarding the PSO operating principle in greater depth.

2.4. Grey Wolf Optimization (GWO)

Grey wolf optimization is based on the rigid hierarchy of grey wolves' hunting behavior [79]. An alpha (α) group, consisting of a small number of males and females, makes major decisions such as hunting and is considered the ideal solution. The second level of the pack, which makes choices and follows orders from the alpha wolves, is known as beta (β). When alphas die or are too old and must be replaced, the best candidate is a female beta. Delta (δ) wolves are the third level of wolves, and they serve as sentinels and scouts and are used in the hunt. Omega (ω), the final level of the pack, is considered the most vulnerable and is tasked with keeping an eye on the young wolves. Grey wolf hunting was described by Muro et al. [115] in three stages: (a) recognizing, following and closing in on the target; (b) encircling the target; and (c) charging the target. These distinct social behaviors are treated by the GWO algorithm as separate variables to consider. A good

starting point for this algorithm's modeling stage is alpha, followed by beta, delta and omega. Detailed information about GWO can be found in Mirjalili et al. [79].

2.5. Equilibrium Optimizer (EO)

Faramarzi et al. [75] were the first to present an EO algorithm based on dynamic mass balance. The concentration of a nonreactive component in a control volume can be determined using various source and sink methods according to the EO methodology. For the preservation of mass entering, leaving and producing, mass balance equations are essential. Every particle (solution) in EO is a search agent, and its concentration (position) determines how effective the search is. To achieve equilibrium, the search agents randomly adjust their concentration to the best-so-far solutions, namely the equilibrium candidates (optimal result). The ability of EO to conduct exploration, exploitation and local minima avoidance is supported by a well-defined concept of "generation rate". The main advantage of EO is that it has a straightforward framework that is easy to implement.

2.6. Harris Hawks Optimization (HHO)

Using SI-based optimization, Heidari et al. [83] developed HHO, a method that relates the hunting habits of Harris hawks to computer systems. Attacking prey (typically rabbits) from multiple directions and employing dynamic and sophisticated strategies that adapt to the prey's fleeing pattern results in exhausted, bewildered prey. There are three steps to the algorithm. An exploratory phase is the first step, in which the birds represent possible solutions; they chase the chosen challenge and make observations. The prey's type and energy determine the second step, which is the transition from exploration to exploitation. In the third step, the identified prey is assaulted and besieged from all sides during the exploitation process. The energy level of the prey, which is determined in the second stage, determines the difficulty of the siege.

2.7. Slime Mold Algorithm (SMA)

Meta-heuristics are influenced by nature, such as with SMA [84], which was developed recently and incorporates mathematical simulations of slime mold propagation waves that determine the optimal path for connecting foodstuffs. Slime mold, a eukaryotic organism found in nature, uses multiple food sources simultaneously to build a venous network connecting said food sources; this mold has unique characteristics and patterns. Slime mold can reach a size of over 900 cm² if it is provided with enough food. The bio-oscillator creates a spreading wave that boosts the cytoplasmic flow into the veins, resulting in thicker veins by increasing the pace of cytoplasmic flow. In light of both its positive and negative reactions, slime may serve as an optimal conduit for food interaction. Since the wave propagation of slime mold has been replicated mathematically through the use of path networks and graph theory, the code has also been modeled in this way. Slime molds can also alter their dynamic search patterns based on the quality of the food they eat. One level of the slime mold algorithm is based on the behavior of slime when acquiring food based on the smell of the air, and the other level is based on the behavior of slime when it executes the contraction of its venous structure when food is warped around it. The initial work by Li et al. [84] provides comprehensive information about SMA, including the basic theory behind it.

2.8. Hybridization Procedure for SVMs and OAs

SVR parameters must be properly defined in order for the model to be successfully implemented and for good performance to be achieved. It is necessary to discover the global optimal solution to attain the greatest possible performance in order to ensure the accuracy of the SVR model's performance. This can be considered an optimization problem. The SVR model's two key parameters (the regularization parameter (γ) and the penalty factor (C)) were found using metaheuristic techniques. Choosing the optimum SVM settings is not possible without additional data. Model identification (the search for parameters)

is, therefore, an important step. The algorithms proposed here were evaluated based on the RMSE value in the training stage to predict unknown data with sufficient accuracy and with minimal error between the predicted and target variables. In the exponential space, the parameters γ and C were explored. Five hybrid models (SVM-PSO, SVM-GWO, SVM-EO, SVM-HHO and SVM-SMA) were created by combining the SVR model with the metaheuristic algorithms PSO, GWO, EO, HHO and SMA.

3. Data Processing and Analysis

3.1. Descriptive Statistics and Statistical Analysis

A collection of 136 experimental results for the single-lap shear test was obtained from previous studies by Moghaddas and Mostofinejad [116], as reported by [58]; these results were used to develop a hybridized SVM model. The specimens were prepared such that FRP laminates were bonded to a concrete prism with the help of grooves, as shown in Figure 1b. Subsequently, the samples were subjected to the single-lap shear test. The elastic modulus of FRP multiplied by the thickness of the fiber ($E_f t_f$, GPa-mm), which is also known as the axial stiffness; the width of the FRP (b_f , mm); the concrete's compressive strength (f_c , MPa); the width of the groove (b_g , mm) and the depth of the groove (h_g , mm) were all been utilized as input variables, while the ultimate capacity (P , KN) was regarded a target variable to train the hybrid models. Table 1 shows the descriptive statistics of the input and output parameters, where it can be seen that the $E_f t_f$ varies from 12.90 to 78.20 with a skewness of 0.58, b_f varies from 60 to 6270, b_g and h_g vary from 10 to 1405, f_c varies from 48.20 to 4585.40 and the output value p varies from 4.76 to 25.49 with a skewness of 0.80; these values indicate the wide variety of experimental data. Statistical analysis was undertaken in order to measure the degree of correlation (DOC) using the Pearson correlation (Figure 3) between the above parameters after the descriptive analysis described above. Statistical analysis revealed that the collected database had a wide range of experimental data. When all parameters were evaluated, the DOCs between p and other parameters (excluding $E_f t_f$ and b_f) were smaller, according to the information provided by the Pearson correlation in Figure 3. The DOCs between p and both $E_f t_f$ and b_f were, on the other hand, shown to be significantly higher. Hence, the availability of a wide range of data, as seen from descriptive analysis, confirms that it can be utilized as an input parameter for the desired output.

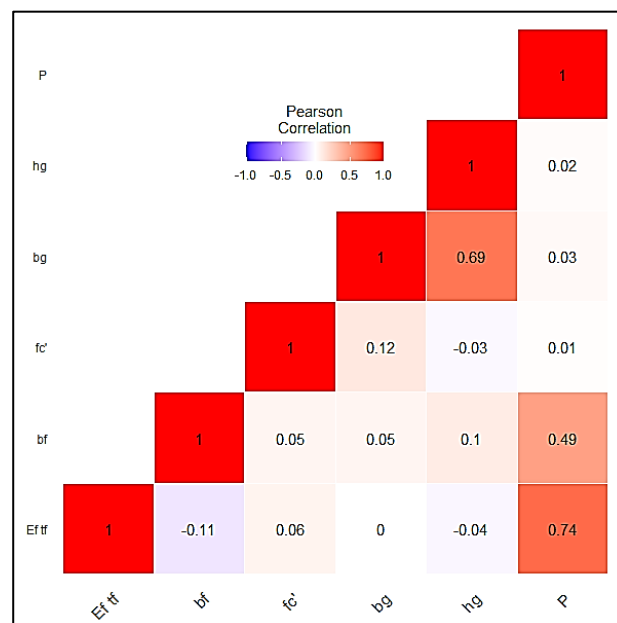


Figure 3. Pearson correlation with heat map.

Table 1. Descriptive statistics of the collected dataset.

Descriptive Statistic	Inputs					Target Variable
	Elastic Modulus of FRP × Thickness of FRP, $E_f t_f$	Width of FRP, b_f	Concrete Compressive Strength, f_c	Width of Groove, b_g	Depth of Groove, h_g	Ultimate Capacity, p
Unit	GPa × mm	mm	Mpa	mm	mm	KN
Mean	40.33	46.10	33.72	7.94	10.33	12.05
Standard Error	2.18	1.01	0.73	0.21	0.30	0.37
Median	39.10	50.00	32.70	10.00	10.00	11.11
Mode	78.20	60.00	26.70	10.00	10.00	9.87
Standard Deviation	25.41	11.81	8.49	2.47	3.45	4.32
Sample Variance	645.42	139.52	72.15	6.10	11.93	18.65
Kurtosis	−1.23	−1.49	−1.11	−1.90	−0.88	0.30
Skewness	0.58	−0.13	0.49	−0.36	−0.09	0.80
Range	65.30	30.00	25.50	5.00	10.00	20.73
Minimum	12.90	30.00	22.70	5.00	5.00	4.76
Maximum	78.20	60.00	48.20	10.00	15.00	25.49
Sum	5484.80	6270.00	4585.40	1080.00	1405.00	1638.72
Count	136.00	136.00	136.00	136.00	136.00	136.00
Confidence Level (95.0%)	4.31	2.00	1.44	0.42	0.59	0.73

3.2. Performance Parameters

Eight different performance indices (Equations (3)–(10)), namely the determination coefficient (R^2), the performance index (PI), the variance account factor (VAF), Willmott's index of agreement (WI), the root mean square error (RMSE), the mean absolute error (MAE), the RMSE observation standard deviation ratio (RSR) and the weighted mean absolute percentage error (WMAPE), were determined to evaluate the performance of the developed models [38,44,117–133]. For a flawless prediction model, the values of these indices should be identical to their ideal values, as shown in Table 2. Note that the generalization capacity of any predictive model is evaluated by determining various metrics, such as the degree of correlation, the associated error, the amount of variation, etc., from these diverse aspects.

$$R^2 = \frac{\sum_{i=1}^n (y_i - y_{mean})^2 - \sum_{i=1}^n (y_i - \hat{y}_i)^2}{\sum_{i=1}^n (y_i - y_{mean})^2} \quad (3)$$

$$PI = adj.R^2 + 0.01VAF - RMSE \quad (4)$$

$$VAF (\%) = \left(1 - \frac{var(y_i - \hat{y}_i)}{var(y_i)}\right) \times 100 \quad (5)$$

$$WI = 1 - \left[\frac{\sum_{i=1}^n (y_i - \hat{y}_i)^2}{\sum_{i=1}^n \{|\hat{y}_i - y_{mean}| + |y_i - y_{mean}|\}^2} \right] \quad (6)$$

$$RMSE = \sqrt{\frac{1}{n} \sum_{i=1}^n (y_i - \hat{y}_i)^2} \quad (7)$$

$$MAE = \frac{1}{n} \sum_{i=1}^n |(\hat{y}_i - y_i)| \quad (8)$$

$$RSR = \frac{RMSE}{\sqrt{\frac{1}{n} \sum_{i=1}^n (y_i - y_{mean})^2}} \quad (9)$$

$$WMAPE = \frac{\sum_{i=1}^n \left| \frac{y_i - \hat{y}_i}{y_i} \right| \times y_i}{\sum_{i=1}^n y_i} \tag{10}$$

where y_i is the actual value, \hat{y}_i is the predicted value and y_{mean} is the mean of the actual value.

Table 2. Ideal values of different performance parameters.

Indices	R ²	PI	VAF	WI	RMSE	MAE	RSR	WMAPE
Ideal Value	1	2	100	1	0	0	0	0

4. Results and Discussion

4.1. Parametric Configuration

As mentioned earlier, to construct optimum hybrid models, it is necessary to prespecify the hyper-parameters of the SVM. The values of γ and C were set (using trial and error) as shown in Table 3 for different hybrid SVM models. Following a trial-and-error approach, the most appropriate values for the swarm size (N_S) and the number of iterations (Itr) were set at 30 and 200, respectively, and were kept constant for other hybrid SVM models. It is also important to note that the convergence behavior of any OA is essential when evaluating performance. This is because the convergence behavior exposes the ability of OAs to break out of local minima and arrive at a faster solution. Figure 4 exhibits the convergence curves that were calculated using the hybrid models that were built. All of the models constructed are compared here in terms of the best and worst convergence behaviors. It can be concluded from the Figure 4 that the best model in terms of convergence was SVM-EO and the worst was SVM-SMA.

Table 3. Parametric configuration of hybrid SVM models.

Models	SVM-PSO	SVM-GWO	SVM-EO	SVM-HHO	SVM-SMA
N_S	30	30	30	30	30
Itr	200	200	200	200	200
C	0.05	0.10064	0.1	12.5253	71.2704
γ	8.73	100	100	99.3516	71.2704

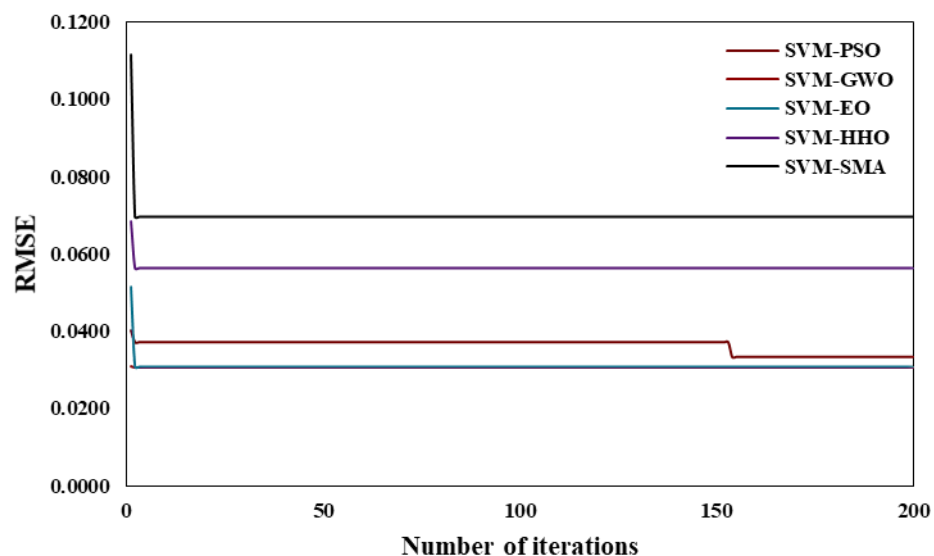


Figure 4. Convergence behavior of hybrid SVM models.

Five-fold cross-validation was performed for both the training and testing phases, as shown in Tables 4 and 5. However, the model was selected based on the lowest RMSE achieved in the testing phase. From Table 5, it can be observed that the SVM–HHO achieved an RMSE of 0.0642, which was the lowest among all the cross-validations in the testing phase.

Table 4. Performance of five-fold cross-validation (training phase).

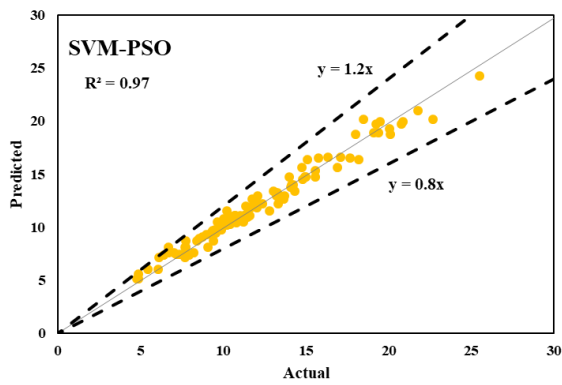
Phase	TR	TR	TR	TR	TR
Models	CV-1	CV-2	CV-3	CV-4	CV-5
SVM–PSO	0.0334	0.0531	0.0561	0.0553	0.0549
SVM–GWO	0.0307	0.0474	0.0499	0.0492	0.0500
SVM–EO	0.0307	0.0474	0.0500	0.0492	0.0500
SVM–HHO	0.0563	0.0571	0.0600	0.0613	0.0550
SVM–SMA	0.0697	0.0696	0.0754	0.0773	0.0691

Table 5. Performance of five-fold cross-validation (testing phase).

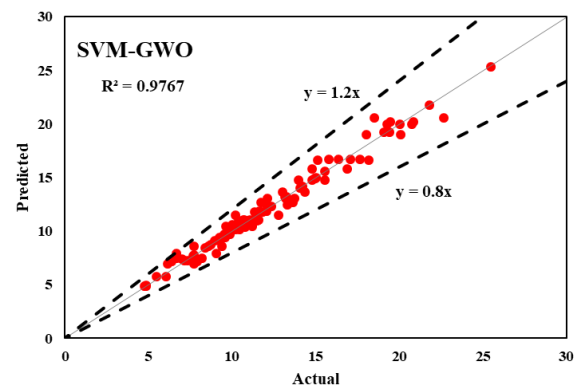
Phase	TS	TS	TS	TS	TS
Models	CV-1	CV-2	CV-3	CV-4	CV-5
SVM–PSO	0.0936	0.1090	0.0979	0.0688	0.0953
SVM–GWO	0.0829	0.1078	0.0944	0.0688	0.0654
SVM–EO	0.0830	0.1078	0.0942	0.0786	0.0765
SVM–HHO	0.0642	0.1012	0.0981	0.0833	0.0915
SVM–SMA	0.0820	0.0993	0.1029	0.0777	0.0835

4.2. Model Performance

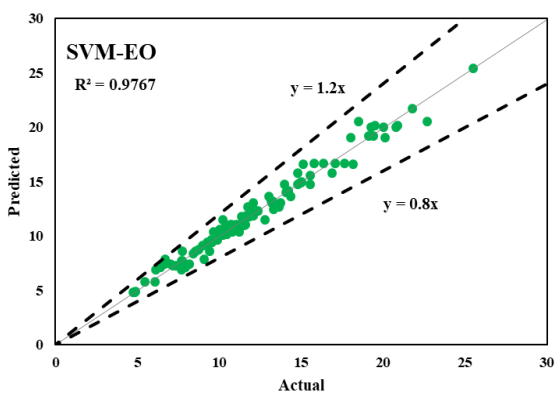
The predictive outcomes of the developed hybrid SVM models for estimating the interfacial bond strength of externally bonded FRP laminates are presented in this section. The performance of the models in predicting the training and testing outputs are reported in Tables 6 and 7, respectively. It should be noted that each model's performance with the training subset was used to express the goodness of fit of the constructed models. Based on the experimental results, SVM–GWO and SVM–EO attained the highest R^2 and the lowest RMSE values ($R^2 = 0.9774$ and $RMSE = 0.0307$), respectively, in the training phase. Among the developed hybrid SVM models, SVM–HHO attained the most desired accuracy, with an R^2 of 0.9294 and an RMSE of 0.0642 in the training phase. On the other hand, SVM–HHO achieved a prediction performance of $R^2 = 0.9241$ and $RMSE = 0.0563$ in testing. These findings demonstrate that, among the proposed hybrid models, SVM–HHO had good predictive performance in both phases of prediction. In addition, the MAE and WMAPE values of the developed SVM–HHO were determined to be 0.0414 and 0.1169 in training and 0.0520 and 0.1507 in testing, respectively. SVM–GWO and SVM–EO were next-best compared to the above model in training ($MAE = 0.0217$ and $WMAPE = 0.0614$), and SVM–SMA was the second-best model ($MAE = 0.0647$ and $WMAPE = 0.1876$) in testing. SVM–SMA and SVM–PSO were the worst performing models compared to others in both training and testing. The same results are reported in Figures 5 and 6, which depict the actual versus predicted graphs for both phases.



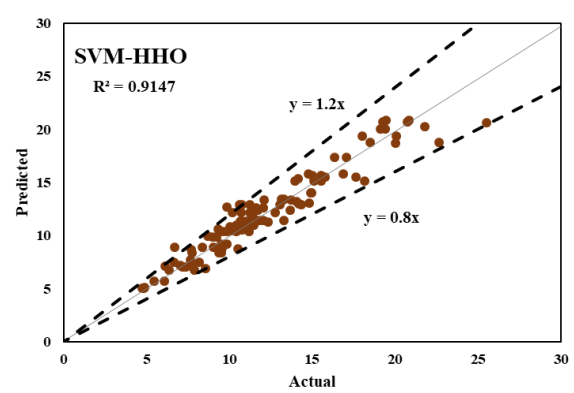
(a)



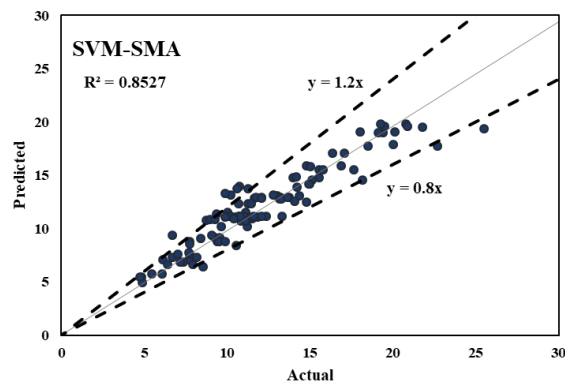
(b)



(c)

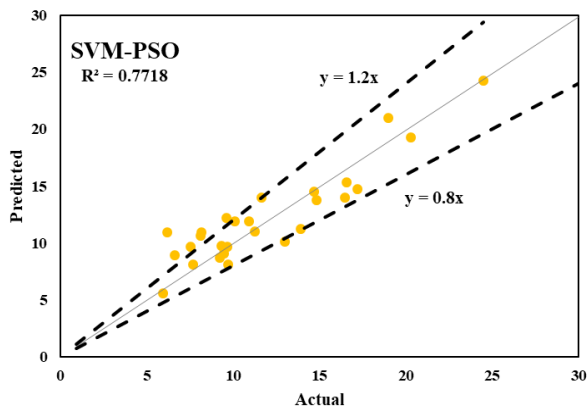


(d)

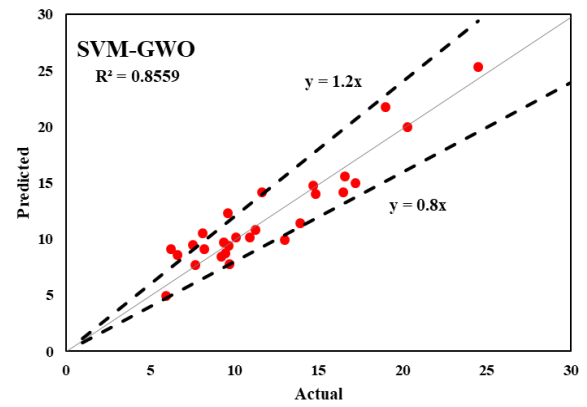


(e)

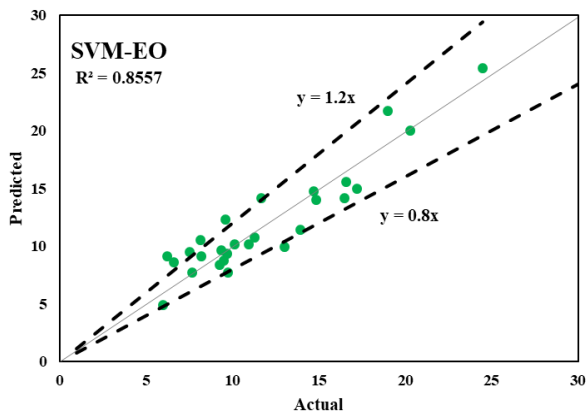
Figure 5. Actual vs. predicted graphs for the training dataset; (a) SVM-PSO (b) SVM-GWO (c) SVM-EO (d) SVM-HHO (e) SVM-SMA.



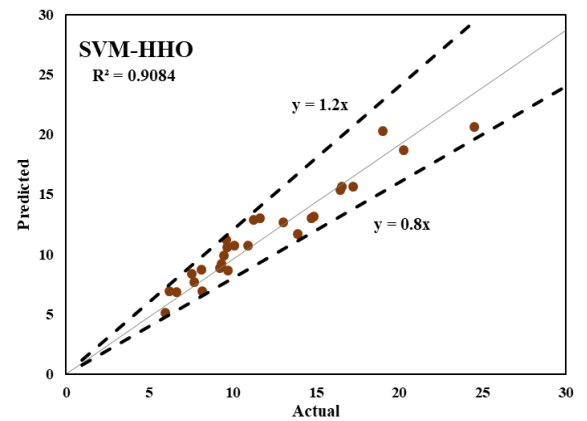
(a)



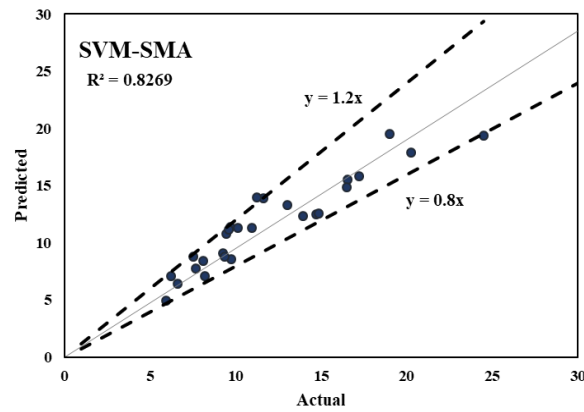
(b)



(c)



(d)



(e)

Figure 6. Actual vs. predicted graphs for the testing dataset; (a) SVM-PSO (b) SVM-GWO (c) SVM-EO (d) SVM-HHO (e) SVM-SMA.

Table 6. Performance indices for the training dataset.

Indices	SVM-PSO	SVM-GWO	SVM-EO	SVM-HHO	SVM-SMA
R ²	0.9763	0.9774	0.9774	0.9241	0.8870
PI	1.9151	1.9229	1.9229	1.7877	1.6949
VAF	97.3227	97.7341	97.7343	92.3648	88.3036
WI	0.9928	0.9942	0.9942	0.9794	0.9661
RMSE	0.0334	0.0307	0.0307	0.0563	0.0697
MAE	0.0260	0.0217	0.0217	0.0414	0.0504
RSR	0.1636	0.1505	0.1505	0.2763	0.3420
WMAPE	0.0730	0.0614	0.0614	0.1169	0.1417

Table 7. Performance indices for the testing dataset.

Indices	SVM-PSO	SVM-GWO	SVM-EO	SVM-HHO	SVM-SMA
R ²	0.8270	0.8633	0.8631	0.9294	0.8794
PI	1.5185	1.6082	1.6078	1.7690	1.6356
VAF	82.6247	86.0428	86.0258	92.0625	86.6904
WI	0.9480	0.9635	0.9634	0.9757	0.9580
RMSE	0.0936	0.0829	0.0830	0.0642	0.0820
MAE	0.0758	0.0675	0.0676	0.0520	0.0647
RSR	0.4216	0.3737	0.3739	0.2895	0.3694
WMAPE	0.2196	0.1957	0.1958	0.1507	0.1876

4.3. Taylor Diagrams

As demonstrated in Figures 7 and 8, the Taylor diagram can be used to study the performance of the hybrid SVM models for both the training and testing datasets [134]. The ability of the models to predict the intended output is determined by this diagram. For the relative quantification of the models, we look at three different statistical metrics (RMSE, correlation coefficients and standard deviation ratios). The center RMSE (the distance from the measured point) is taken as the reference point. The standard deviation and correlation coefficient are both set to 1 for the reference model. On the graph, it can be seen that the standard deviation and correlation coefficient values for all five hybrid models were close to 1 for the training phase. It can be concluded from the graph that SVM-SMA had the lowest correlation in training, whereas both SVM-GWO and SVM-EO showed the best performance in the training phase. For the testing dataset, the SVM-HHO model performed the best among all five models, followed by SVM-SMA, SM-GWO and SVM-EO. Hence, it can be concluded that the overall best-performing model was SVM-HHO as it provided good results for both training and testing.

4.4. Regression Error Characteristic Curve

The regression error characteristic (REC) curve plots the graph of error tolerance versus the percentage of predicted points that fall inside the tolerance. The x and y axes show the regression function's tolerance for errors and its accuracy, respectively. The area over the REC curve (AOC) serves as a good approximation of the projected inaccuracy. The better a model performs, the lower the AOC. Thus, the ROC curve provides a visual representation of a model's performance that is both quick and precise. Figures 9 and 10 show the REC curves for both stages of the models. A visual interpretation alone shows that SVM-SMA was the least accurate model in the training phase in terms of the accuracy of prediction. We compare the AOC values of different models in order to see how well they function. Table 8 depicts the AOC results. The SVM-GWO and SVM-EO models outperformed the competition during the training phase (with an AOC value of 0.4407); for testing, the SVM-HHO model outperformed the others with an AOC value of 0.0486. For SVM-GWO and SVM-EO, the lines virtually overlap (the black and green lines), and the AOC values were also the same for both training and testing.

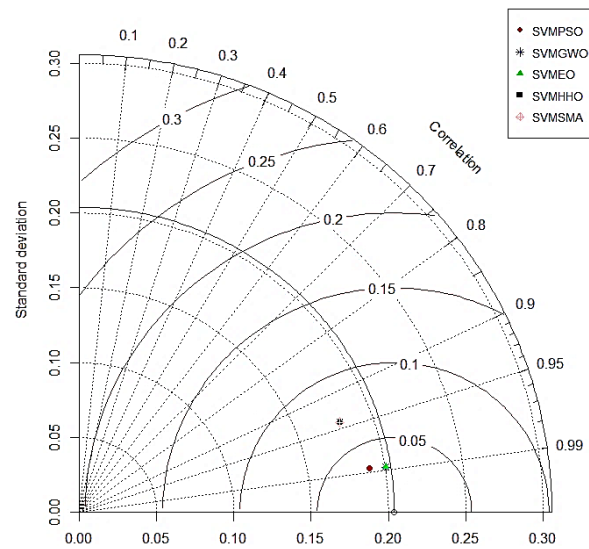


Figure 7. Taylor diagram for the training results.

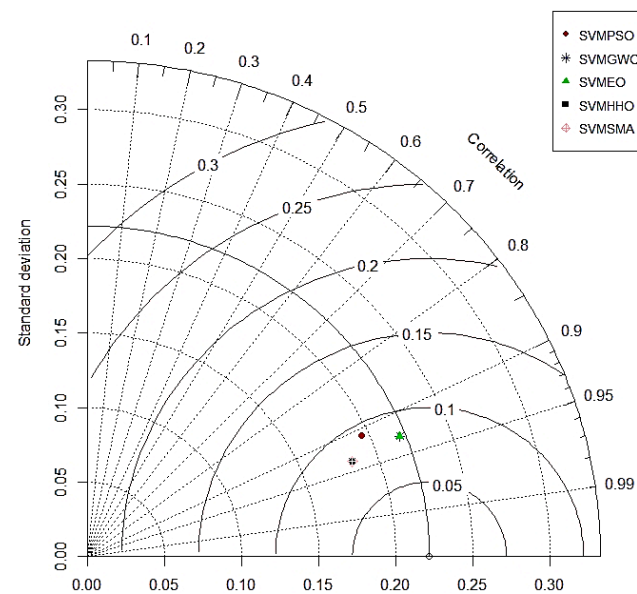


Figure 8. Taylor diagram for the testing results.

Table 8. Values of AOC.

Model	AOC Value	
	Training	Testing
SVM-PSO	0.5264	0.0716
SVM-GWO	0.4407	0.0648
SVM-EO	0.4407	0.0648
SVM-HHO	0.8358	0.0486
SVM-SMA	1.0158	0.0601

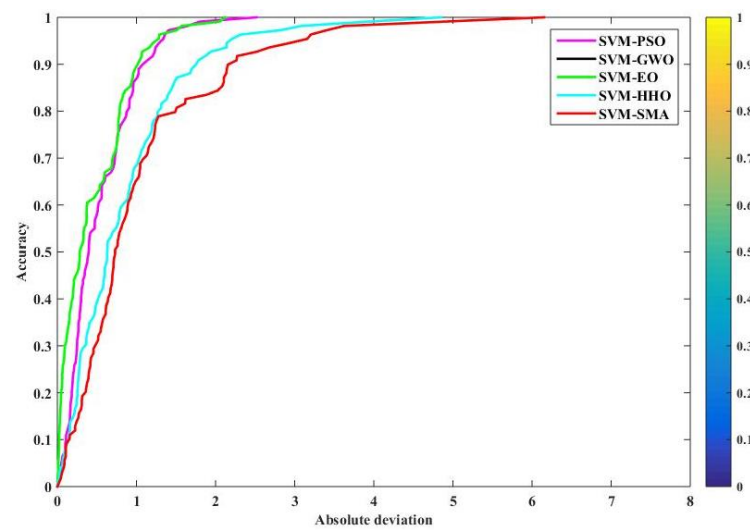


Figure 9. REC curves for training.

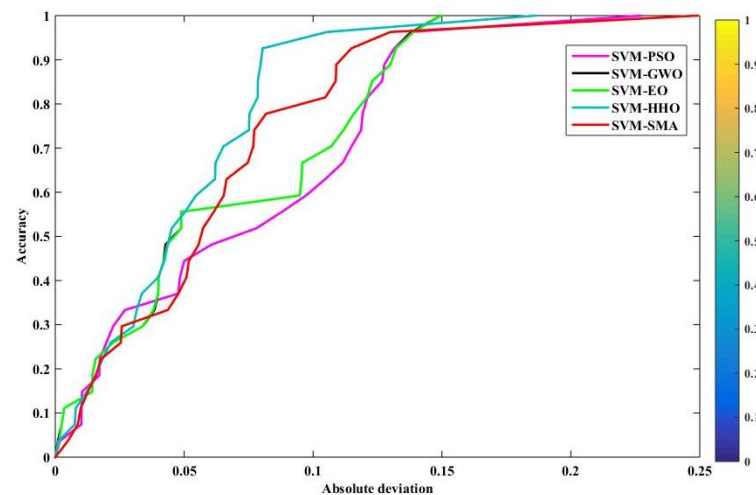


Figure 10. REC curves for testing.

5. Conclusions

It is relevant to mention that an accurate and trustworthy prediction of the interfacial bond strength of FRP laminates bonded on grooves with concrete prisms will make the construction process more economical. In the current study, a collection of 136 experimental SST datasets with five input parameters was obtained from a literature survey. Some recently developed MOAs were employed in the creation of models using an SVM. Among the models, SVM-GWO and SVM-EO ($R^2 = 0.9774$, $RSME = 0.0307$, $WI = 0.9942$) were the best performing models in the training stage, followed by SVM-PSO and SVM-HHO; SVM-HHO ($R^2 = 0.9294$, $RSME = 0.0642$, $WI = 0.9757$) was the best performing model in the testing stage. In addition, SVM-SMA and SVM-PSO were the most underperforming models in the training and testing phases, respectively. The experimental validation of SVM-HHO demonstrates that it has a higher prediction accuracy in both the training and testing stages. These results are significantly better than those obtained from other hybrid SVMs. Based on the experimental outcomes, the proposed SVM-HHO has the potential to assist structural engineers in estimating the ultimate capacity of FRP during the design phase of civil engineering projects. Similar results were also obtained via analysis using Taylor diagrams and REC curves. It is important to note that this study only illustrated the performance efficiency of the models; however, the authors opine that subsequent studies should present detailed parametric and sensitivity analyses for the practical implications of

FRP laminates. For now, engineers may use the dataset of the reported study to train the SVM–HHO hybrid model to test new data related to the bond strength of FRP laminates bonded to concrete prisms. However, since this study used hybrid SVM models to predict the bond strength of externally bonded FRP laminates, therefore, the future direction of related work may include the development of an empirical engineering model for a comparative assessment.

Author Contributions: Conceptualization, K.K., M.I. and R.B.; methodology, M.N.A., S.A., M.I. and R.B.; software, J.G. and R.B.; validation, A.A.A., R.B. and M.I.; formal analysis, A.M.A.A.; investigation, M.N.A. and K.K.; resources, K.K., M.N.A. and A.A.A.; data curation, M.I. and K.K.; writing—original draft preparation, R.B., J.G. and S.A.; writing—review and editing, M.N.A., R.B., M.I. and K.K.; visualization, R.B. and J.G.; supervision, M.N.A. and K.K.; project administration, M.N.A. and M.I.; funding acquisition, M.N.A. and K.K. All authors have read and agreed to the published version of the manuscript.

Funding: This work was supported by the Deanship of Scientific Research, Vice Presidency for Graduate Studies and Scientific Research, King Faisal University, Saudi Arabia [Project No. GRANT102].

Institutional Review Board Statement: Not applicable.

Informed Consent Statement: Not applicable.

Data Availability Statement: The data used in this research have been properly cited and reported in the main text.

Acknowledgments: The authors acknowledge the Deanship of Scientific Research, Vice Presidency for Graduate Studies and Scientific Research, King Faisal University, Saudi Arabia [Project No. GRANT102].

Conflicts of Interest: The authors declare no conflict of interest.

References

1. Liberati, E.A.P.; Nogueira, C.G.; Leonel, E.D.; Chateaufneuf, A. Nonlinear formulation based on FEM, Mazars damage criterion and Fick's law applied to failure assessment of reinforced concrete structures subjected to chloride ingress and reinforcements corrosion. *Eng. Fail. Anal.* **2014**, *46*, 247–268. [[CrossRef](#)]
2. Siddika, A.; al Mamun, M.A.; Ferdous, W.; Alyousef, R. Performances, challenges and opportunities in strengthening reinforced concrete structures by using FRPs—A state-of-the-art review. *Eng. Fail. Anal.* **2020**, *111*, 104480. [[CrossRef](#)]
3. Yang, J.; Haghani, R.; Blanksvärd, T.; Lundgren, K. Experimental study of FRP-strengthened concrete beams with corroded reinforcement. *Constr. Build. Mater.* **2021**, *301*, 124076. [[CrossRef](#)]
4. Panahi, M.; Zareei, S.A.; Izadi, A. Flexural strengthening of reinforced concrete beams through externally bonded FRP sheets and near surface mounted FRP bars. *Case Stud. Constr. Mater.* **2021**, *15*, e00601. [[CrossRef](#)]
5. Kotynia, R.; Oller, E.; Mari, A.; Kaszubska, M. Efficiency of shear strengthening of RC beams with externally bonded FRP materials—State-of-the-art in the experimental tests. *Compos. Struct.* **2021**, *267*, 113891. [[CrossRef](#)]
6. Abedini, M.; Zhang, C. Dynamic performance of concrete columns retrofitted with FRP using segment pressure technique. *Compos. Struct.* **2021**, *260*, 113473. [[CrossRef](#)]
7. Hadi, M.N.S. Behaviour of FRP strengthened concrete columns under eccentric compression loading. *Compos. Struct.* **2007**, *77*, 92–96. [[CrossRef](#)]
8. Tafsirojjaman, T.; Fawzia, S.; Thambiratnam, D.P.; Zhao, X.L. FRP strengthened SHS beam-column connection under monotonic and large-deformation cyclic loading. *Thin-Walled Struct.* **2021**, *161*, 107518. [[CrossRef](#)]
9. Lee, W.T.; Chiou, Y.J.; Shih, M.H. Reinforced concrete beam-column joint strengthened with carbon fiber reinforced polymer. *Compos. Struct.* **2010**, *92*, 48–60. [[CrossRef](#)]
10. Wu, Y.-F.; Jiang, C. Quantification of Bond-Slip Relationship for Externally Bonded FRP-to-Concrete Joints. *J. Compos. Constr.* **2013**, *17*, 673–686. [[CrossRef](#)]
11. Fathelbab, F.A.; Ramadan, M.S.; Al-Tantawy, A. Strengthening of RC bridge slabs using CFRP sheets. *Alex. Eng. J.* **2014**, *53*, 843–854. [[CrossRef](#)]
12. Xian, G.; Guo, R.; Li, C. Combined effects of sustained bending loading, water immersion and fiber hybrid mode on the mechanical properties of carbon/glass fiber reinforced polymer composite. *Compos. Struct.* **2021**, *281*, 115060. [[CrossRef](#)]
13. Ding, J.; Cheng, L.; Chen, X.; Chen, C.; Liu, K. A review on ultra-high cycle fatigue of CFRP. *Compos. Struct.* **2021**, *256*, 113058. [[CrossRef](#)]
14. Guo, R.; Xian, G.; Li, F.; Li, C.; Hong, B. Hygrothermal resistance of pultruded carbon, glass and carbon/glass hybrid fiber reinforced epoxy composites. *Constr. Build. Mater.* **2021**, *315*, 125710. [[CrossRef](#)]

15. Zhang, S.S.; Yu, T.; Chen, G.M. Reinforced concrete beams strengthened in flexure with near-surface mounted (NSM) CFRP strips: Current status and research needs. *Compos. Part B Eng.* **2017**, *131*, 30–42. [[CrossRef](#)]
16. Ghorbani, M.; Mostofinejad, D.; Hosseini, A. Experimental investigation into bond behavior of FRP-to-concrete under mixed-mode I/II loading. *Constr. Build. Mater.* **2017**, *132*, 303–312. [[CrossRef](#)]
17. Bakay, R.; Shrive, N.G.; Sayed-Ahmed, E.Y. Bond Strength of FRP Laminates to Concrete: State-of-the-Art Review. *Electron. J. Struct. Eng.* **2009**, *9*, 45–61.
18. Teng, T.; Chen, J.; Yu, J.-F. *FRP-Strengthened RC Structures*; John Wiley & Sons Ltd.: Hoboken, NJ, USA, 2002.
19. Nguyen, B.D.M.; Chan, T.K.; Cheong, H.K. Brittle Failure and Bond Development Length of Cfrp-Concrete Beams. *J. Compos. Constr.* **2001**, *5*, 12–17. [[CrossRef](#)]
20. Lu, Z.; Xian, G.; Li, H. Effects of exposure to elevated temperatures and subsequent immersion in water or alkaline solution on the mechanical properties of pultruded BFRP plates. *Compos. Part B Eng.* **2015**, *77*, 421–430. [[CrossRef](#)]
21. Smith, S.T.; Teng, J.G. FRP-strengthened RC beams. I: Review of debonding strength models. *Eng. Struct.* **2002**, *24*, 385–395. [[CrossRef](#)]
22. Wan, B.; Jiang, C.; Wu, Y.F. Effect of defects in externally bonded FRP reinforced concrete. *Constr. Build. Mater.* **2018**, *172*, 63–76. [[CrossRef](#)]
23. Chajes, M.J.; Finch, W.W.; Januszka, T.F.; Thomson, T.A. Bond and force transfer of composite material plates bonded to concrete. *ACI Struct. J.* **1996**, *93*, 208–217. [[CrossRef](#)]
24. Jiang, C.; Wan, B.; Wu, Y.F.; Omboko, J. Epoxy interlocking: A novel approach to enhance FRP-to-concrete bond behavior. *Constr. Build. Mater.* **2018**, *193*, 643–653. [[CrossRef](#)]
25. Kishore, K.; Gupta, N. Mechanical characterization and assessment of composite geopolymer concrete. *Mater. Today Proc.* **2021**, *44*, 58–62. [[CrossRef](#)]
26. Tiwari, P.K.; Sharma, P.; Sharma, N.; Verma, M.; Rohitash. An experimental investigation on metakaoline GGBS based concrete with recycled coarse aggregate. *Mater. Today Proc.* **2020**, *43*, 1025–1030. [[CrossRef](#)]
27. Parashar, A.K.; Gupta, N.; Kishore, K.; Nagar, P.A. An experimental investigation on mechanical properties of calcined clay concrete embedded with bacillus subtilis. *Mater. Today Proc.* **2021**, *44*, 129–134. [[CrossRef](#)]
28. Mostofinejad, D.; Mahmoudabadi, E. Grooving as Alternative Method of Surface Preparation to Postpone Debonding of FRP Laminates in Concrete Beams. *J. Compos. Constr.* **2010**, *14*, 804–811. [[CrossRef](#)]
29. Bencardino, F.; Condello, A.; Ashour, A.F. Single-lap shear bond tests on Steel Reinforced Geopolymeric Matrix-concrete joints. *Compos. Part B Eng.* **2017**, *110*, 62–71. [[CrossRef](#)]
30. Mofrad, M.H.; Mostofinejad, D.; Hosseini, A. A generic non-linear bond-slip model for CFRP composites bonded to concrete substrate using EBR and EBROG techniques. *Compos. Struct.* **2019**, *220*, 31–44. [[CrossRef](#)]
31. Al-Jaberi, Z.; Myers, J.J.; Chandrashekhara, K. Effect of direct service temperature exposure on the bond behavior between advanced composites and CMU using NSM and EB techniques. *Compos. Struct.* **2019**, *211*, 63–75. [[CrossRef](#)]
32. Yuan, H.; Teng, J.G.; Seracino, R.; Wu, Z.S.; Yao, J. Full-range behavior of FRP-to-concrete bonded joints. *Eng. Struct.* **2004**, *26*, 553–565. [[CrossRef](#)]
33. Figiel, Ł.; Kamiński, M. Numerical probabilistic approach to sensitivity analysis in a fatigue delamination problem of a two layer composite. *Appl. Math. Comput.* **2009**, *209*, 75–90. [[CrossRef](#)]
34. Carrara, P.; Ferretti, D. A finite-difference model with mixed interface laws for shear tests of FRP plates bonded to concrete. *Compos. Part B Eng.* **2013**, *54*, 329–342. [[CrossRef](#)]
35. Bardhan, A.; Samui, P.; Ghosh, K.; Gandomi, A.H.; Bhattacharyya, S. ELM-based adaptive neuro swarm intelligence techniques for predicting the California bearing ratio of soils in soaked conditions. *Appl. Soft Comput.* **2021**, *110*, 107595. [[CrossRef](#)]
36. Biswas, R.; Samui, P.; Rai, B. Determination of compressive strength using relevance vector machine and emotional neural network. *Asian J. Civ. Eng.* **2019**, *20*, 1109–1118. [[CrossRef](#)]
37. Kumar, S.; Rai, B.; Biswas, R.; Samui, P.; Kim, D. Prediction of rapid chloride permeability of self-compacting concrete using Multivariate Adaptive Regression Spline and Minimax Probability Machine Regression. *J. Build. Eng.* **2020**, *32*, 101490. [[CrossRef](#)]
38. Biswas, R.; Rai, B. Effect of cementing efficiency factor on the mechanical properties of concrete incorporating silica fume. *J. Struct. Integr. Maint.* **2020**, *5*, 190–203. [[CrossRef](#)]
39. Biswas, R.; Rai, B.; Samui, P.; Roy, S.S. Estimating concrete compressive strength using MARS, LSSVM and GP. *Eng. J.* **2020**, *24*, 41–52. [[CrossRef](#)]
40. Biswas, R.; Bardhan, A.; Samui, P.; Rai, B.; Nayak, S.; Armaghani, D.J. Efficient soft computing techniques for the prediction of compressive strength of geopolymer concrete. *Comput. Concr.* **2021**, *28*, 221–232. [[CrossRef](#)]
41. Khan, M.A.; Memon, S.A.; Farooq, F.; Javed, M.F.; Aslam, F.; Alyousef, R. Compressive Strength of Fly-Ash-Based Geopolymer Concrete by Gene Expression Programming and Random Forest. *Adv. Civ. Eng.* **2021**, *2021*, 6618407. [[CrossRef](#)]
42. Khan, M.I.; Sutanto, M.H.; Khan, K.; Iqbal, M.; Bin Napiyah, M.; Zoorob, S.E.; Klemeš, J.J.; Bokhari, A.; Rafiq, W. Effective use of recycled waste PET in cementitious grouts for developing sustainable semi-flexible pavement surfacing using artificial neural network (ANN). *J. Clean. Prod.* **2022**, *340*, 130840. [[CrossRef](#)]
43. Iqbal, M.; Zhang, D.; Jalal, F.E.; Javed, M.F. Computational AI prediction models for residual tensile strength of GFRP bars aged in the alkaline concrete environment. *Ocean. Eng.* **2021**, *232*, 109134. [[CrossRef](#)]

44. Iqbal, M.; Zhao, Q.; Zhang, D.; Jalal, F.E.; Jamal, A. Evaluation of tensile strength degradation of GFRP rebars in harsh alkaline conditions using non-linear genetic-based models. *Mater. Struct. Mater. Constr.* **2021**, *54*, 190. [[CrossRef](#)]
45. Jalal, F.E.; Xu, Y.; Iqbal, M.; Jamhiri, B.; Javed, M.F. Predicting the compaction characteristics of expansive soils using two genetic programming-based algorithms. *Transp. Geotech.* **2021**, *30*, 100608. [[CrossRef](#)]
46. Aamir, M.; Tolouei-Rad, M.; Vafadar, A.; Raja, M.N.A.; Giasin, K. Performance analysis of multi-spindle drilling of Al2024 with TiN and TiCN coated drills using experimental and artificial neural networks technique. *Appl. Sci.* **2020**, *10*, 8633. [[CrossRef](#)]
47. Khan, M.U.A.; Shukla, S.K.; Raja, M.N.A. Soil–conduit interaction: An artificial intelligence application for reinforced concrete and corrugated steel conduits. *Neural Comput. Appl.* **2021**, *33*, 14861–14885. [[CrossRef](#)]
48. Khan, M.U.A.; Shukla, S.K.; Raja, M.N.A. Load-settlement response of a footing over buried conduit in a sloping terrain: A numerical experiment-based artificial intelligent approach. *Soft Comput.* **2022**, *26*, 6839–6856. [[CrossRef](#)]
49. Zhang, W.; Zhang, R.; Goh, A.T.C. Multivariate adaptive regression splines approach to estimate lateral wall deflection profiles caused by braced excavations in clays. *Geotech. Geol. Eng.* **2018**, *36*, 1349–1363. [[CrossRef](#)]
50. Zhang, W.; Zhang, Y.; Goh, A.T.C. Multivariate adaptive regression splines for inverse analysis of soil and wall properties in braced excavation. *Tunn. Undergr. Space Technol.* **2017**, *64*, 24–33. [[CrossRef](#)]
51. Bhatti, U.N.; Khan, S.; Ali, S.; Horoub, M.M. A Numerical Modeling Study of The Effects of Various Joint Boundary Conditions on Stiffness Behavior of 6DOF Platform's Top Plate. In Proceedings of The 2018 9th International Conference on Mechanical and Aerospace Engineering (ICMAE), Budapest, Hungary, 10–13 July 2018; pp. 243–248. [[CrossRef](#)]
52. Horoub, M.M.; Khan, S.; Ali, S.; Horoub, A.M. Comparative Analysis of a Floating Mooring Line-Driven Platform (FMDP) Having Different Mooring Lines Patterns. In Proceedings of the 2018 9th International Conference on Mechanical and Aerospace Engineering (ICMAE), Budapest, Hungary, 10–13 July 2018; pp. 269–273. [[CrossRef](#)]
53. Hawwa, M.A.; Ali, S.; Hardt, D.E. Influence of roll-to-roll system's dynamics on axially moving web vibration. *J. Vibroengineering* **2019**, *21*, 556–569. [[CrossRef](#)]
54. Dubey, P.; Gupta, N. Experimental Investigation on Strength and Durability of Concrete with Partial Replacement of Cement Using Calcined Clay. In *Calcined Clays for Sustainable Concrete*; RILEM Bookseries; Springer: Singapore, 2020; Volume 25, pp. 713–722. [[CrossRef](#)]
55. Vu, D.T.; Hoang, N.D. Punching shear capacity estimation of FRP-reinforced concrete slabs using a hybrid machine learning approach. *Struct. Infrastruct. Eng.* **2016**, *12*, 1153–1161. [[CrossRef](#)]
56. Hoang, N.D. Estimating punching shear capacity of steel fibre reinforced concrete slabs using sequential piecewise multiple linear regression and artificial neural network. *Meas. J. Int. Meas. Confed.* **2019**, *137*, 58–70. [[CrossRef](#)]
57. Abuodeh, O.R.; Abdalla, J.A.; Hawileh, R.A. Prediction of shear strength and behavior of RC beams strengthened with externally bonded FRP sheets using machine learning techniques. *Compos. Struct.* **2020**, *234*, 111698. [[CrossRef](#)]
58. Su, M.; Zhong, Q.; Peng, H.; Li, S. Selected machine learning approaches for predicting the interfacial bond strength between FRPs and concrete. *Constr. Build. Mater.* **2021**, *270*, 121456. [[CrossRef](#)]
59. Kecman, V. *Learning and Soft Computing: Support Vector Machines, Neural Networks, and Fuzzy Logic Models*; MIT Press: Cambridge, MA, USA, 2001.
60. Lu, M.; AbouRizk, S.M.; Hermann, U.H. Sensitivity Analysis of Neural Networks in Spool Fabrication Productivity Studies. *J. Comput. Civ. Eng.* **2001**, *15*, 299–308. [[CrossRef](#)]
61. Samui, P. Support vector machine applied to settlement of shallow foundations on cohesionless soils. *Comput. Geotech.* **2008**, *35*, 419–427. [[CrossRef](#)]
62. Vapnik, V.; Golowich, S.E.; Smola, A. Support vector method for function approximation, regression estimation, and signal processing. *Adv. Neural Inf. Process. Syst.* **1997**, *9*, 281–287.
63. Pal, M.; Deswal, S. Support vector regression based shear strength modelling of deep beams. *Comput. Struct.* **2011**, *89*, 1430–1439. [[CrossRef](#)]
64. Mita, A.; Hagiwara, H. Quantitative damage diagnosis of shear structures using support vector machine. *KSCE J. Civ. Eng.* **2003**, *7*, 683–689. [[CrossRef](#)]
65. Farfani, H.A.; Behnamfar, F.; Fathollahi, A. Dynamic analysis of soil-structure interaction using the neural networks and the support vector machines. *Expert Syst. Appl.* **2015**, *42*, 8971–8981. [[CrossRef](#)]
66. Gunn, S.R.; Brown, M.; Bossley, K.M. Network performance assessment for neurofuzzy data modelling. In *International Symposium on Intelligent Data Analysis*; Lecture Notes in Computer Science (Including Subseries Lecture Notes in Artificial Intelligence and Lecture Notes in Bioinformatics); Springer: Berlin/Heidelberg, Germany, 1997; Volume 1280, pp. 313–323. [[CrossRef](#)]
67. Abualigah, L.; Diabat, A. Advances in Sine Cosine Algorithm: A comprehensive survey. *Artif. Intell. Rev.* **2021**, *54*, 2567–2608. [[CrossRef](#)]
68. Abualigah, L.; Diabat, A. A comprehensive survey of the Grasshopper optimization algorithm: Results, variants, and applications. *Neural Comput. Appl.* **2020**, *32*, 15533–15556. [[CrossRef](#)]
69. Abualigah, L. Group search optimizer: A nature-inspired meta-heuristic optimization algorithm with its results, variants, and applications. *Neural Comput. Appl.* **2021**, *33*, 2949–2972. [[CrossRef](#)]
70. Abualigah, L. Multi-verse optimizer algorithm: A comprehensive survey of its results, variants, and applications. *Neural Comput. Appl.* **2020**, *32*, 12381–12401. [[CrossRef](#)]
71. Yao, X.; Liu, Y.; Lin, G. Evolutionary programming made faster. *IEEE Trans. Evol. Comput.* **1999**, *3*, 82–102. [[CrossRef](#)]

72. Michalewicz, Z. Evolution Strategies and Other Methods. Genetic Algorithms, Data Structures and Evolution Programs. Available online: https://link.springer.com/chapter/10.1007/978-3-662-03315-9_9 (accessed on 1 June 2022).
73. Goldberg, D.E.; Holland, J.H. Genetic algorithms and Machine Learning. *Mach. Learn.* **1988**, *3*, 95–99. [[CrossRef](#)]
74. Storn, R.; Price, K. Differential Evolution—A Simple and Efficient Heuristic for Global Optimization over Continuous Spaces. *J. Glob. Optim.* **1997**, *11*, 341–359. [[CrossRef](#)]
75. Koza, U.; John, R. Genetic programming as a means for programming computers by natural selection. *Stat. Comput.* **1994**, *4*, 87–112. [[CrossRef](#)]
76. Eberhart, R.; Sixth, J.K. A new optimizer using particle swarm theory. In Proceedings of the IEEE Symposium on Micro Machine and Human Science, Nagoya, Japan, 4–6 October 1995; pp. 39–43.
77. Karaboga, D.; Basturk, B. Artificial Bee Colony (ABC) optimization algorithm for solving constrained optimization problems. In *Foundations of Fuzzy Logic and Soft Computing*; Lecture Notes in Computer Science (Including Subseries Lecture Notes in Artificial Intelligence and Lecture Notes in Bioinformatics); Springer: Berlin/Heidelberg, Germany, 2007; Volume 4529, pp. 789–798. [[CrossRef](#)]
78. Mirjalili, S.; Mirjalili, S.M.; Lewis, A. Grey Wolf Optimizer. *Adv. Eng. Softw.* **2014**, *69*, 46–61. [[CrossRef](#)]
79. Blum, C. Ant colony optimization: Introduction and recent trends. *Phys. Life Rev.* **2005**, *2*, 353–373. [[CrossRef](#)]
80. Mirjalili, S.; Gandomi, A.H.; Mirjalili, S.Z.; Saremi, S.; Faris, H.; Mirjalili, S.M. Salp Swarm Algorithm: A bio-inspired optimizer for engineering design problems. *Adv. Eng. Softw.* **2017**, *114*, 163–191. [[CrossRef](#)]
81. Faramarzi, A.; Heidarinejad, M.; Mirjalili, S.; Gandomi, A.H. Marine Predators Algorithm: A nature-inspired metaheuristic. *Expert Syst. Appl.* **2020**, *152*, 113377. [[CrossRef](#)]
82. Heidari, A.A.; Mirjalili, S.; Faris, H.; Aljarah, I.; Mafarja, M.; Chen, H. Harris hawks optimization: Algorithm and applications. *Future Gener. Comput. Syst.* **2019**, *97*, 849–872. [[CrossRef](#)]
83. Li, S.; Chen, H.; Wang, M.; Heidari, A.A.; Mirjalili, S. Slime mould algorithm: A new method for stochastic optimization. *Future Gener. Comput. Syst.* **2020**, *111*, 300–323. [[CrossRef](#)]
84. Mirjalili, S.; Lewis, A. The Whale Optimization Algorithm. *Adv. Eng. Softw.* **2016**, *95*, 51–67. [[CrossRef](#)]
85. Tamura, K.; Yasuda, K. Primary study of spiral dynamics inspired optimization. *IEEJ Trans. Electr. Electron. Eng.* **2011**, *6*, S98–S100. [[CrossRef](#)]
86. Eskandar, H.; Sadollah, A.; Bahreininejad, A.; Hamdi, M. Water cycle algorithm—A novel metaheuristic optimization method for solving constrained engineering optimization problems. *Comput. Struct.* **2012**, *110–111*, 151–166. [[CrossRef](#)]
87. Shah-Hosseini, H. Intelligent water drops algorithm: A new optimization method for solving the multiple knapsack problem. *Int. J. Intell. Comput. Cybern.* **2008**, *1*, 193–212. [[CrossRef](#)]
88. Kaveh, A. Field of Forces Optimization. In *Advances in Metaheuristic Algorithms for Optimal Design of Structures*; Springer: Cham, Switzerland, 2017; pp. 139–160. [[CrossRef](#)]
89. Abedinpourshotorban, H.; Shamsuddin, S.M.; Beheshti, Z.; Jawawi, D.N.A. Electromagnetic field optimization: A physics-inspired metaheuristic optimization algorithm. *Swarm Evol. Comput.* **2016**, *26*, 8–22. [[CrossRef](#)]
90. Kaveh, A. Advances in Metaheuristic Algorithms for Optimal Design of Structures. In *Advances in Metaheuristic Algorithms for Optimal Design of Structures*; Springer: Cham, Switzerland, 2021. [[CrossRef](#)]
91. Birbil, Ş.I.; Fang, S.C. An electromagnetism-like mechanism for global optimization. *J. Glob. Optim.* **2003**, *25*, 263–282. [[CrossRef](#)]
92. Kaveh, A.; Talatahari, S. A novel heuristic optimization method: Charged system search. *Acta Mech.* **2010**, *213*, 267–289. [[CrossRef](#)]
93. Rashedi, E.; Nezamabadi-pour, H.; Saryazdi, S. GSA: A Gravitational Search Algorithm. *Inf. Sci.* **2009**, *179*, 2232–2248. [[CrossRef](#)]
94. Kirkpatrick, S.; Gelatt, C.D.; Vecchi, M.P. Optimization by simulated annealing. *Science* **1983**, *220*, 671–680. [[CrossRef](#)] [[PubMed](#)]
95. Abualigah, L.; Yousri, D.; Elaziz, M.A.; Ewees, A.A.; Al-qaness, M.A.A.; Gandomi, A.H. Aquila Optimizer: A novel meta-heuristic optimization algorithm. *Comput. Ind. Eng.* **2021**, *157*, 107250. [[CrossRef](#)]
96. Tahani, M.; Babayan, N. Flow Regime Algorithm (FRA): A physics-based meta-heuristics algorithm. *Knowl. Inf. Syst.* **2019**, *60*, 1001–1038. [[CrossRef](#)]
97. Kashan, A.H. A new metaheuristic for optimization: Optics inspired optimization (OIO). *Comput. Oper. Res.* **2015**, *55*, 99–125. [[CrossRef](#)]
98. Lam, A.Y.S.; Li, V.O.K. Chemical-reaction-inspired metaheuristic for optimization. *IEEE Trans. Evol. Comput.* **2010**, *14*, 381–399. [[CrossRef](#)]
99. Abualigah, L.; Elaziz, M.A.; Hussien, A.G.; Alsalihi, B.; Jalali, S.M.J.; Gandomi, A.H. Lightning search algorithm: A comprehensive survey. *Appl. Intell.* **2021**, *51*, 2353–2376. [[CrossRef](#)]
100. Rao, R.V.; Savsani, V.J.; Vakharia, D.P. Teaching-learning-based optimization: A novel method for constrained mechanical design optimization problems. *CAD Comput. Aided Des.* **2011**, *43*, 303–315. [[CrossRef](#)]
101. Moghdani, R.; Salimifard, K. Volleyball Premier League Algorithm. *Appl. Soft Comput. J.* **2018**, *64*, 161–185. [[CrossRef](#)]
102. Moosavian, N.; Roodsari, B.K. Soccer league competition algorithm: A novel meta-heuristic algorithm for optimal design of water distribution networks. *Swarm Evol. Comput.* **2014**, *17*, 14–24. [[CrossRef](#)]
103. Chaohua, D.; Weirong, C.; Yunfang, Z. Seeker optimization algorithm. In Proceedings of the 2006 International Conference on Computational Intelligence and Security, ICCIAS, Guangzhou, China, 3–6 November 2006; Volume 1, pp. 225–229. [[CrossRef](#)]
104. Kashan, A.H. League Championship Algorithm: A new algorithm for numerical function optimization. In Proceedings of the SoCPaR 2009—Soft Computing and Pattern Recognition, Malacca, Malaysia, 4–7 December 2009; pp. 43–48. [[CrossRef](#)]

105. Kumar, M.; Kulkarni, A.J.; Satapathy, S.C. Socio evolution & learning optimization algorithm: A socio-inspired optimization methodology. *Future Gener. Comput. Syst.* **2018**, *81*, 252–272. [[CrossRef](#)]
106. Cortes, C.; Vapnik, V. Support-vector networks. *Mach. Learn.* **1995**, *20*, 273–297. [[CrossRef](#)]
107. Karimi, Y.; Prasher, S.O.; Patel, R.M.; Kim, S.H. Application of support vector machine technology for weed and nitrogen stress detection in corn. *Comput. Electron. Agric.* **2006**, *51*, 99–109. [[CrossRef](#)]
108. Trebar, M.; Steele, N. Application of distributed SVM architectures in classifying forest data cover types. *Comput. Electron. Agric.* **2008**, *63*, 119–130. [[CrossRef](#)]
109. Li, Q.; Yang, B.; Li, Y.; Deng, N.; Jing, L. Constructing support vector machine ensemble with segmentation for imbalanced datasets. *Neural Comput. Appl.* **2013**, *22*, 249–256. [[CrossRef](#)]
110. Moayedi, H.; Hayati, S. Artificial intelligence design charts for predicting friction capacity of driven pile in clay. *Neural Comput. Appl.* **2019**, *31*, 7429–7445. [[CrossRef](#)]
111. Samui, P.; Dixon, B. Application of support vector machine and relevance vector machine to determine evaporative losses in reservoirs. *Hydrol. Process.* **2012**, *26*, 1361–1369. [[CrossRef](#)]
112. Kennedy, J.; Eberhart, R. Particle swarm optimization. In Proceedings of the ICNN'95-International Conference on Neural Networks, Perth, WA, Australia, 27 November–1 December 1995; pp. 1942–1948.
113. Bui, D.T.; Nhu, V.H.; Hoang, N.D. Prediction of soil compression coefficient for urban housing project using novel integration machine learning approach of swarm intelligence and Multi-layer Perceptron Neural Network. *Adv. Eng. Inform.* **2018**, *38*, 593–604. [[CrossRef](#)]
114. Muro, C.; Escobedo, R.; Spector, L.; Coppinger, R.P. Wolf-pack (*Canis lupus*) hunting strategies emerge from simple rules in computational simulations. *Behav. Process.* **2011**, *88*, 192–197. [[CrossRef](#)]
115. Moghaddas, A.; Mostofinejad, D. Empirical FRP-concrete bond strength model for externally bonded reinforcement on grooves. *J. Compos. Constr.* **2019**, *23*, 04018080. [[CrossRef](#)]
116. Kardani, N.; Bardhan, A.; Kim, D.; Samui, P.; Zhou, A. Modelling the energy performance of residential buildings using advanced computational frameworks based on RVM, GMDH, ANFIS-BBO and ANFIS-IPSO. *J. Build. Eng.* **2021**, *35*, 102105. [[CrossRef](#)]
117. Bardhan, A.; GuhaRay, A.; Gupta, S.; Pradhan, B.; Gokceoglu, C. A novel integrated approach of ELM and modified equilibrium optimizer for predicting soil compression index of subgrade layer of Dedicated Freight Corridor. *Transp. Geotech.* **2022**, *32*, 100678. [[CrossRef](#)]
118. Das, G.; Burman, A.; Bardhan, A.; Kumar, S.; Choudhary, S.S.; Samui, P. Risk estimation of soil slope stability problems. *Arab. J. Geosci.* **2022**, *15*, 204. [[CrossRef](#)]
119. Bardhan, A.; Biswas, R.; Kardani, N.; Iqbal, M.; Samui, P.; Singh, M.P.; Asteris, P.G. A novel integrated approach of augmented grey wolf optimizer and ANN for estimating axial load carrying-capacity of concrete-filled steel tube columns. *Constr. Build. Mater.* **2022**, *337*, 127454. [[CrossRef](#)]
120. Pradeep, T.; Bardhan, A.; Burman, A.; Samui, P. Rock Strain Prediction Using Deep Neural Network and Hybrid Models of ANFIS and Meta-Heuristic Optimization Algorithms. *Infrastructures* **2021**, *6*, 129. [[CrossRef](#)]
121. Kaloop, M.R.; Bardhan, A.; Kardani, N.; Samui, P.; Hu, J.W.; Ramzy, A. Novel application of adaptive swarm intelligence techniques coupled with adaptive network-based fuzzy inference system in predicting photovoltaic power. *Renew. Sustain. Energy Rev.* **2021**, *148*, 111315. [[CrossRef](#)]
122. Bardhan, A.; Kardani, N.; GuhaRay, A.; Burman, A.; Samui, P.; Zhang, Y. Hybrid ensemble soft computing approach for predicting penetration rate of tunnel boring machine in a rock environment. *J. Rock Mech. Geotech. Eng.* **2021**, *13*, 1398–1412. [[CrossRef](#)]
123. Pradeep, T.; Bardhan, A.; Samui, P. Prediction of rock strain using soft computing framework. *Innov. Infrastruct. Solut.* **2022**, *7*, 37. [[CrossRef](#)]
124. Kardani, N.; Bardhan, A.; Samui, P.; Nazem, M.; Asteris, P.G.; Zhou, A. Predicting the thermal conductivity of soils using integrated approach of ANN and PSO with adaptive and time-varying acceleration coefficients. *Int. J. Therm. Sci.* **2022**, *173*, 107427. [[CrossRef](#)]
125. Bardhan, A.; Kardani, N.; Alzo'ubi, A.K.; Samui, P.; Gandomi, A.H.; Gokceoglu, C. A Comparative Analysis of Hybrid Computational Models Constructed with Swarm Intelligence Algorithms for Estimating Soil Compression Index. *Arch. Comput. Methods Eng.* **2022**, 1–39. [[CrossRef](#)]
126. Bardhan, A.; Manna, P.; Kumar, V.; Burman, A.; Zlender, B.; Samui, P. Reliability Analysis of Piled Raft Foundation Using a Novel Hybrid Approach of ANN and Equilibrium Optimizer. *CMES-Comput. Model. Eng. Sci.* **2021**, *128*, 1033–1067. [[CrossRef](#)]
127. Asteris, P.G.; Skentou, A.D.; Bardhan, A.; Samui, P.; Lourenço, P.B. Soft computing techniques for the prediction of concrete compressive strength using Non-Destructive tests. *Constr. Build. Mater.* **2021**, *303*, 124450. [[CrossRef](#)]
128. Bardhan, A.; Samui, P. Application of Artificial Intelligence Techniques in Slope Stability Analysis: A Short Review and Future Prospects. *Int. J. Geotech. Earthq. Eng. (IJGEE)* **2022**, *13*, 1–22. [[CrossRef](#)]
129. Amin, M.N.; Iqbal, M.; Khan, K.; Qadir, M.G.; Shalabi, F.I.; Jamal, A. Ensemble tree-based approach towards flexural strength prediction of frp reinforced concrete beams. *Polymers* **2022**, *14*, 1303. [[CrossRef](#)]
130. Asteris, P.G.; Skentou, A.D.; Bardhan, A.; Samui, P.; Pilakoutas, K. Predicting concrete compressive strength using hybrid ensembling of surrogate machine learning models. *Cem. Concr. Res.* **2021**, *145*, 106449. [[CrossRef](#)]

131. Kardani, N.; Bardhan, A.; Samui, P.; Nazem, M.; Zhou, A.; Armaghani, D.J. A novel technique based on the improved firefly algorithm coupled with extreme learning machine (ELM-IFF) for predicting the thermal conductivity of soil. *Eng. Comput.* **2021**, *1*–20. [[CrossRef](#)]
132. Kumar, M.; Bardhan, A.; Samui, P.; Hu, J.W.; Kaloop, M.R. Reliability Analysis of Pile Foundation Using Soft Computing Techniques: A Comparative Study. *Processes* **2021**, *9*, 486. [[CrossRef](#)]
133. Bardhan, A.; Gokceoglu, C.; Burman, A.; Samui, P.; Asteris, P.G. Efficient computational techniques for predicting the California bearing ratio of soil in soaked conditions. *Eng. Geol.* **2021**, *291*, 106239. [[CrossRef](#)]
134. Taylor, K.E. Summarizing multiple aspects of model performance in a single diagram. *J. Geophys. Res. Atmos.* **2001**, *106*, 7183–7192. [[CrossRef](#)]